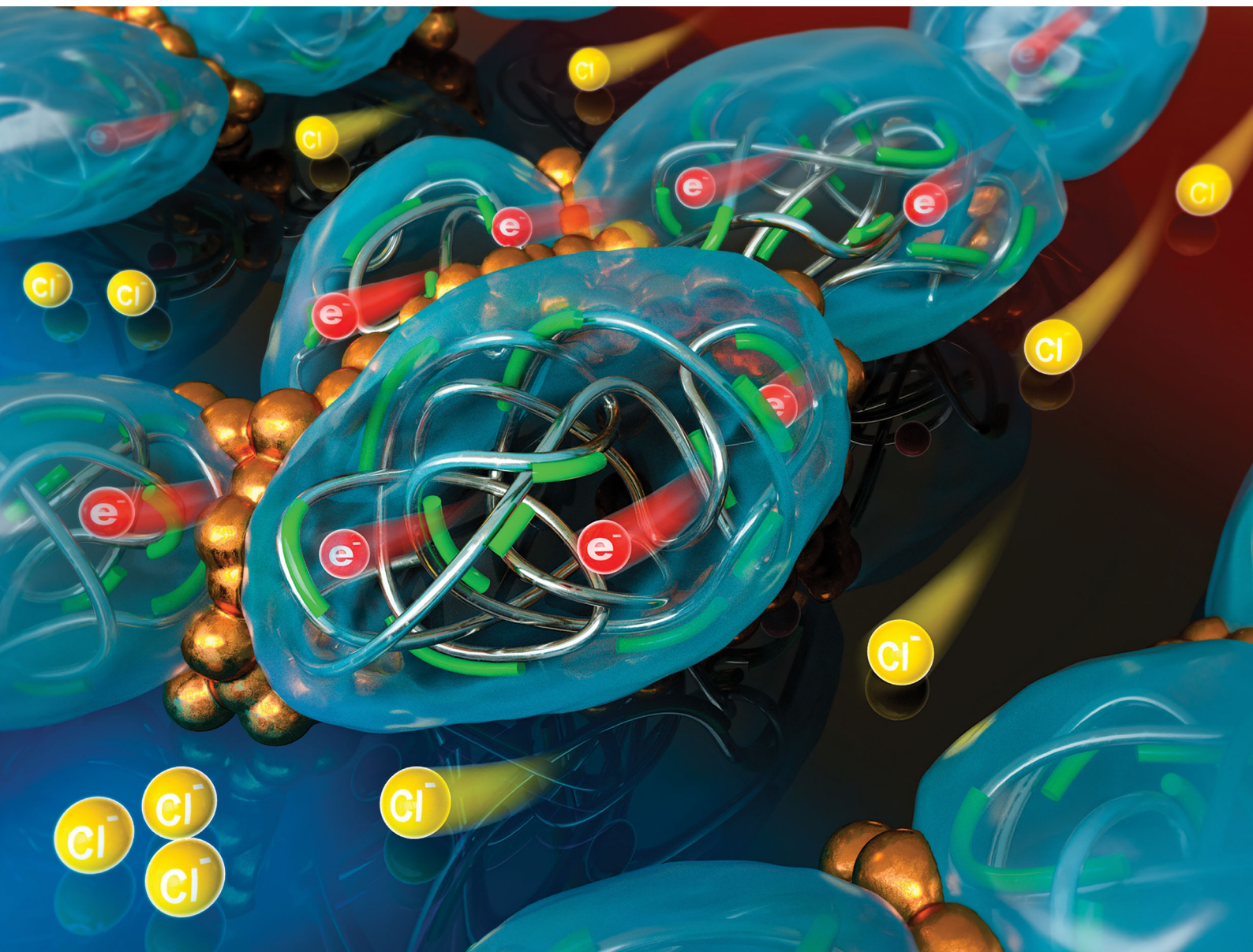


# Energy & Environmental Science

Volume 13  
Number 3  
March 2020  
Pages 651-1040

rsc.li/ees



ISSN 1754-5706

## PAPER

Eunyoung Kim *et al.*  
Chloride transport in conductive polymer films for an n-type  
thermoelectric platform

PAPER

View Article Online  
View Journal | View Issue



Cite this: *Energy Environ. Sci.*,  
2020, 13, 859

# Chloride transport in conductive polymer films for an n-type thermoelectric platform†

Byeonggwon Kim,<sup>id</sup> Jong Un Hwang and Eunkyong Kim<sup>id</sup> \*

$\text{Cl}^-$  transport in a conductive polymer (CP) film was demonstrated for n-type thermoelectric (TE) harvesting. CPs have been considered as an important group of p-type TE materials due to their high TE functionalities plus simple processing steps for a device. In particular, recently emerging p-type ionic CPs can be unique candidates due to their high Seebeck coefficients ( $S$ ). However, n-type materials based on CPs suffer from very poor TE functionalities, and n-type ionic TE CP materials have not been realized so far. Here, we report the first example of n-type mixed ionic–electronic CP composite (NPC) films. The p-type TE properties of the PEDOT:PSS films was drastically converted into the n-type TE properties in the presence of  $\text{CuCl}_2$  through metal binding with polymers, thus resulting in the formation of  $\text{Cl}^-$  channels. Fluorescence imaging using  $\text{Cl}^-$  as an indicator and time-of-flight secondary ion mass spectrometry mapping confirmed that  $\text{Cl}^-$  is transported in the film from the hot to the cold electrode. In addition, electron spin resonance spectroscopy indicated the major spin density transition from a polaron of PEDOT:PSS to the polymer-bound unpaired electron spin of Cu ions by increasing the  $\text{CuCl}_2$  content to prove the binding of metal ions with the PSS unit of the polymer chain. These mixed ionic–electronic NPC films recorded a surprisingly high negative  $S$  value of over  $-18.2 \text{ mV K}^{-1}$  and a power factor of  $1.7 \text{ mW m}^{-1} \text{ K}^{-2}$  at 80% RH with 40 wt% of  $\text{CuCl}_2$ . Taking advantage of this high performance, the CP films were integrated with a p-type CP film as a flexible module-type TE harvester with 10 pairs of p–n legs on CNT electrodes. This TE harvester showed a thermovoltage of 1.55 V for a low temperature gradient of 4.5 K. This high anion transport in a TE CP hydrogel film might be a useful solution for environmentally benign and body-worn electronics.

Received 26th July 2019,  
Accepted 6th November 2019

DOI: 10.1039/c9ee02399b

rsc.li/ees

## Broader context

Thermoelectrics harvest electrical energy directly from waste heat through electron and ion transport between the temperature gradient. While TE materials have been explored to provide increased TE output by optimizing molecular and nanostructures, the output from the currently available TE materials is still low because of the difficulties in controlling the carrier transport. In particular, a high TE performance for flexible and low-cost polymeric TE materials is a challenging issue in wearable thermoelectrics. In this work, we tackled this challenge by optimizing the transport of chloride ions as n-type carriers in PEDOT:PSS films, which further benefited from the formation of copper ion-complexed polymer channels. With such a new n-type TE mechanism, the p-type TE property of the PEDOT:PSS film was drastically converted into an n-type TE property. The Seebeck coefficient and power factor of the n-type film were over  $-18 \text{ mV K}^{-1}$  and  $1.7 \text{ mW m}^{-1} \text{ K}^{-2}$ , respectively, which provided flexible module-type thermoelectrics, generating 1.55 V for a small  $\Delta T$  value of 4.5 K. This high anion transport in a polymer film can be useful to power wearable electronics and inspire new strategies for carrier control for mixed ionic–electronic devices.

## Introduction

The importance of  $\text{Cl}^-$  transport has been demonstrated extensively not only for human diseases that are due to mutations in chloride channels but also in the chemical industry for electrochemical

devices, anion exchange membranes, anti-corrosion efforts, and drinking water.<sup>1</sup> The ions flow through the transporter driven by the concentration gradient of the ions or by imposed stimuli. In particular, under a temperature gradient ( $\Delta T$ ), ion transport generates thermoelectric (TE) output, which has emerged as a promising TE mechanism for self-powered bionics, sensors, and renewable energy harvesters.<sup>2–7</sup>

To this end, eco-friendly and low-cost conductive polymers (CPs) have been explored as unique candidates for p-type TE materials due to their high Seebeck coefficients ( $S$ ).<sup>8,9</sup>

Department of Chemical and Biomolecular Engineering, Yonsei University, 50 Yonsei-ro, Seodaemun-gu, Seoul 03722, South Korea. E-mail: eunkim@yonsei.ac.kr

† Electronic supplementary information (ESI) available. See DOI: 10.1039/c9ee02399b



In particular, ionic TE materials based on poly(3,4-ethylenedioxythiophene) (PEDOT) doped with poly(styrene sulfonate) (PSS) were explored for high ionic Seebeck coefficients ( $S_i$ ) originating from the Soret effect.<sup>10–15</sup> Recently, we demonstrated robust p-type proton-conducting polymer films by using high-molecular-weight poly(styrene sulfonic acid) (PSSH) as a dopant.<sup>9</sup> The highly doped PEDOT:PSS containing 30 wt% PSSH (HDH30) recorded high  $S_i$  (16.2 mV K<sup>−1</sup>) and power factor (PF, 7.6 mW m<sup>−1</sup> K<sup>−2</sup>). Furthermore, the introduction of self-humidifying layers including a metal–organic framework (MOF-801) and a hydrogel layer on the HDH30 films afforded an environmentally sustainable TE prototype.

To realize an efficient TE power generator and create high-density organic TE legs, a module-type TE harvester should be made using p- and n-type TE materials that are sandwiched between two electrical contacts.<sup>16</sup> It is important to understand that in ionic thermoelectric materials, the term n-type (or p-type) is used to describe negative (or positive) ions that can dominantly transport through  $\Delta T$ . While many examples are reported for n-type inorganic TE materials, it is difficult to find organic or polymeric n-type TE materials with PF comparable to those of inorganic TE materials. An n-type material based on CPs suffers from very poor TE functionalities, and n-type ionic TE CP materials having high PF (> 1 mW m<sup>−1</sup> K<sup>−2</sup>) have not been realized so far. Various types of hybrid composites made of organic and inorganic TE materials have been reported since the metal coordination n-type polymer poly[K<sub>x</sub>(Ni-ett)] having PF of 66  $\mu$ W m<sup>−1</sup> K<sup>−2</sup> was reported.<sup>17</sup> Some examples include hybrids of single-walled carbon nanotubes (CNTs) and PEDOT:FeCl<sub>4</sub> treated by tetrakis-(dimethylamino)ethylene (PF of  $\sim$ 1050  $\mu$ W m<sup>−1</sup> K<sup>−2</sup>),<sup>18</sup> poly(Ni-ett) film (PF of  $\sim$ 360  $\mu$ W m<sup>−1</sup> K<sup>−2</sup>),<sup>19</sup> benzyl viologen-doped CNT webs (PF of 3.1 mW m<sup>−1</sup> K<sup>−2</sup>),<sup>20</sup> and the hybrid superlattices of TiS<sub>2</sub>/[(hexylammonium)<sub>x</sub>(H<sub>2</sub>O)<sub>y</sub>(DMSO)] (PF of 450  $\mu$ W m<sup>−1</sup> K<sup>−2</sup>).<sup>21</sup> However, few of them are stable under ambient conditions,<sup>22</sup> limiting their practical application. In addition, most of the conductive inorganic or carbon materials have high thermal conductivity ( $\kappa$ ),<sup>20</sup> which results in a low TE figure of merit,  $ZT = PF \times T/\kappa$ , where  $T$  is the absolute temperature of the material. Therefore, in order to realize an efficient TE generator, n-type ionic TE materials could be an alternative.

Recently, an anion-doped conjugated polymeric system was introduced utilizing strong electronic interactions between lone-pair electrons of anions (such as F<sup>−</sup>, OH<sup>−</sup>, AcO<sup>−</sup>, Br<sup>−</sup>, and I<sup>−</sup>) and  $\pi^*$ -orbitals of the  $\pi$ -electron-deficient units (n- $\pi^*$ -interaction), resulting in effective n-doping.<sup>23,24</sup> Thus, tetrabutylammonium fluoride (TBAF) was employed as the n-dopant for chlorinated benzodifurandione-based poly(*p*-phenylene vinylene) (ClBDPPV) to increase  $\sigma$  up to 0.62 S cm<sup>−1</sup>, with an  $S$  of  $-99.2 \pm 9.2$   $\mu$ V K<sup>−1</sup> in air.<sup>25</sup> The results indicate that small anionic salts such as TBAF as n-dopants of conjugated polymers can provide a strategy toward air-stable n-type CPs. However, the PF of the anion-doped TE materials is still very low because the conductivity is low.

To overcome these obstacles, we hypothesized a free anion-transporting CP film in which anion transport channels are formed by binding the counter cations with mixed ionic–electronic

polymers, instead of such strong n- $\pi^*$ -interaction between anions and CPs as discussed above. Moreover, a mixed ionic–electronic system could further enhance TE performance. It has been reported that Cu<sup>2+</sup> binds to PSS in the PEDOT:PSS film and increases the conductivity of the film when doped with Cu<sup>2+</sup>.<sup>26</sup> Thus, in this system, the counter anion channel could be formed and then anions may be easily transported to a cold side as  $\Delta T$  develops. In particular, among the anions, Cl<sup>−</sup> has one of the highest diffusion coefficients of  $2.032 \times 10^{-5}$  cm<sup>2</sup> s<sup>−1</sup> in aqueous solution.<sup>27</sup> Therefore, the addition of CuCl<sub>2</sub> may result in increases in  $S$  and  $\sigma_i$ , leading to increased output voltage ( $V_{out}$ ) and output power under small  $\Delta T$  conditions. With these hypotheses, we embarked on the development of a mixed anionic–electronic TE system.

Herein, we report the first example of n-type mixed ionic–electronic CP films containing CuCl<sub>2</sub>. The p-type nature of the PEDOT:PSS films was drastically converted into the n-type nature in the presence of CuCl<sub>2</sub>. Fluorescence imaging and time-of-flight secondary ion mass spectrometry (ToF-SIMS) mapping confirmed that Cl<sup>−</sup> was transported to the cold side of the film. In addition, electron spin resonance (ESR) spectroscopy indicated a transition from a polaron of the PEDOT:PSS to a free radical of Cu by increasing CuCl<sub>2</sub>, to prove the binding of metal ions with the PSS unit of the polymer chain. These mixed ionic–electronic NPC films recorded a surprisingly high negative  $S$  of over  $-18.2$  mV K<sup>−1</sup> and a PF of 1.7 mW m<sup>−1</sup> K<sup>−2</sup> at 80% RH with 40 wt% of CuCl<sub>2</sub>. A flexible module-type TE harvester with 10 pairs of p–n legs was fabricated to afford 1.55 V of thermovoltage for a low  $\Delta T$  of 4.5 K. This high anion transport in a TE CP hydrogel film might be a useful solution for environmentally benign and body-worn electronics.

## Results and discussion

A schematic diagram of the n-type mixed ionic–electronic TE polymer system is shown in Fig. 1a, in which CPs are doped with metal cations (M<sup>+</sup>), to generate anionic channels. The highly doped PEDOT:PSS (HD) was chosen as a mixed ionic–electronic polymer<sup>2,9</sup> and CuCl<sub>2</sub> as a binding metal plus anion source. To a solution of PEDOT:PSS, anhydrous CuCl<sub>2</sub> was added in concentrations of 14, 25, 36, 40, and 57 wt% (solids content) and dried to afford metal-complexed anionic polymer films, which were named NPC14, NPC25, NPC36, NPC40, and NPC57, respectively.

ESR measurements were carried out to study the CuCl<sub>2</sub> effect on the nature of the charge carriers in the NPC films. Fig. 1b shows ESR spectra of HD and NPCs (CuCl<sub>2</sub> doped HD). For PEDOT:PSS without CuCl<sub>2</sub> the peak at 3357 G with  $g = 2.0011$  can be accounted for by the polarons in the PEDOT:PSS film.<sup>28</sup> The integrated ESR intensity for PEDOT:PSS decreased by 83% following addition of 14 wt% CuCl<sub>2</sub> (NPC14) and there appeared a new broad ESR line at 3078 G with a  $g = 2.1825$ . Since the  $g$ -factor is lower than 2.3,<sup>29</sup> the line could be attributable to the coupling of the unpaired electron spin with PSS. This line became stronger and sharper with increasing CuCl<sub>2</sub> content (Fig. S1, ESI†).



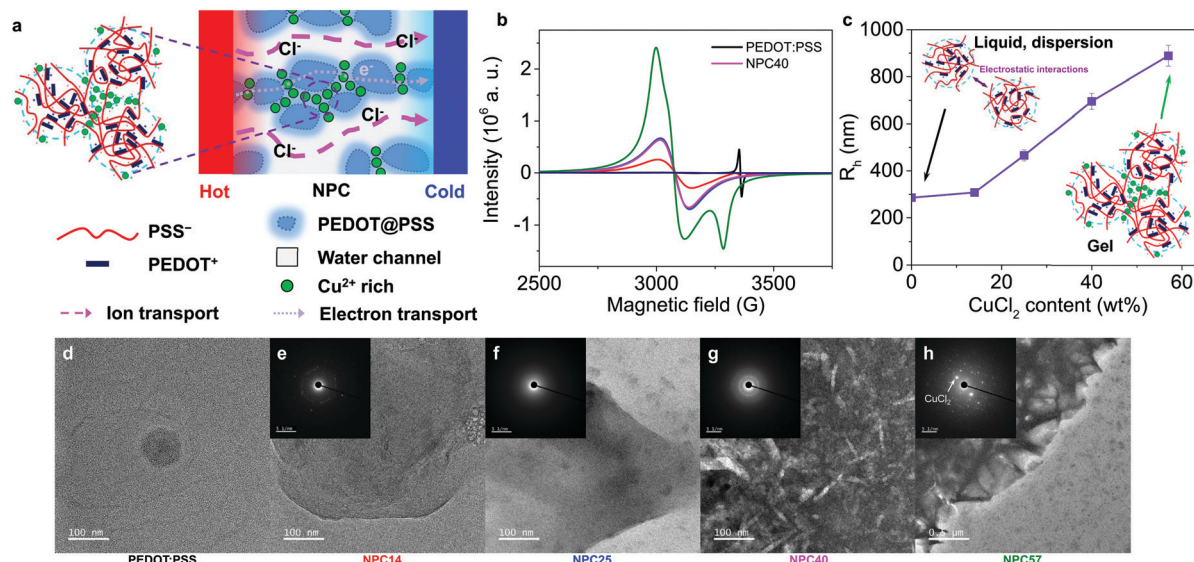


**Fig. 1** Schematic ion transport and morphology of NPC samples. (a) Schematic images of ion carrier transport such as electronic and ionic carriers in the NPC14–NPC57 and PEDOT:PSS films. (b) ESR spectra of NPC and PEDOT:PSS films. PEDOT:PSS (black), NPC14 (red), NPC25 (blue), NPC40 (magenta), NPC57 (green), and PET substrate (navy blue). (c) Hydrodynamic radius ( $R_h$ ) of dilute NPC solutions from DLS measurements. Error bars indicate the s.d. of three experimental replicates. (d–h) TEM images of the NPC films. The inset shows the electron diffraction pattern.

In the presence of excess  $\text{CuCl}_2$  (NPC57), another asymmetric peak was observed at 3285 G, which may be due to the presence of the anisotropic film and Cu isotope. Interestingly, the  $g$ -factors in the NPC14 to NPC40 were almost the same (2.1825–2.1834) and increased slightly in NPC57 ( $g = 2.1960$ ). This indicates that the nature of the spin in the Cu ions that bind to the PSS could be the same.

Fig. S2 (ESI<sup>†</sup>) shows the absorption spectra of NPC films, which show a high bipolaronic absorption of PEDOT at 1610 nm, along with a polaronic band with a maximum at 810 nm. The absorption of the NPC films in the NIR region increased with increasing  $\text{CuCl}_2$  content. Interestingly, the absorbance intensity ( $A_\lambda$ ) in the visible region increased linearly as the  $\text{CuCl}_2$  content increased. This indicates that  $\text{CuCl}_2$  binding to PSS led to partial de-doping in PEDOT. The conductivity of the PEDOT:PSS was increased with increasing  $\text{CuCl}_2$  content, which matches well with a previous report.<sup>26</sup>

From the X-ray photoelectron spectroscopy (XPS) for NPC films, two Cu 2p peaks<sup>30,31</sup> were observed at 932.4 ( $2p_{3/2}$ ) and 951.9 eV ( $2p_{1/2}$ ) (Fig. S3a, ESI<sup>†</sup>). Those two peaks were split into two with a splitting degree of 2.3 eV for both  $2p_{3/2}$  and  $2p_{1/2}$ , which could be associated with  $\text{Cu}^+$  and  $\text{Cu}^{2+}$ , respectively. Additionally, the Cu 2p spectra showed characteristic shake-up satellites peaks. As the  $\text{Cu}^{2+}$  concentration increased in the NPC film, the Cu 2p peaks shifted to lower binding energy, and the integration ratio of  $\text{Cu}^+:\text{Cu}^{2+}$  reached 1:1.08. This means that a small excess of  $\text{Cu}^{2+}$  participated in the binding with polymers in aqueous media. Fig. S3b (ESI<sup>†</sup>) shows two characteristic peaks of S 2p for PSS<sup>-</sup> and PEDOT<sup>+</sup> at binding energies of 168.2 and 164.0 eV, respectively, for NPC40. Similar to the Cu 2p peaks, the S 2p peak of PSS<sup>-</sup> shifted from 168.7 to 168.1 eV as the  $\text{Cu}^{2+}$  concentration increased because  $\text{Cu}^{2+}$  withdraws electron density from PSS<sup>-</sup>. Based on these results, we conclude that the addition

of  $\text{CuCl}_2$  in PEDOT:PSS produces ionic cross-linking between the PSS shell and  $\text{Cu}^{2+}$ . This can be beneficial for the generation of a free anion channel in wet conductive polymer media for the n-type ionic TE effect.

Dynamic light scattering (DLS) measurements of the hydrodynamic radius ( $R_h$ ) for dilute NPC solutions were plotted against solute weight percent, as shown in Fig. 1c and Fig. S4 (ESI<sup>†</sup>). We found that the size of the microgels changed upon  $\text{CuCl}_2$  addition. At 40 and 57 wt%, approximately 14 and 30 dispersed particles aggregated to make a larger particle as a microgel. The zeta potential increased from  $-29$  to  $-13$  mV as the  $\text{Cu}^{2+}$  concentration increased from 0 to 57 wt% (Fig. S4c, ESI<sup>†</sup>). The diffusion of  $\text{Cu}^{2+}$  ions to the electrical double layer near the surface of the PEDOT:PSS nanoparticle resulted in an increase in the zeta potential. Additionally, the solution conductivity increased as the  $\text{Cu}^{2+}$  concentration increased (Fig. S4d, ESI<sup>†</sup>). Further identification of the PSS<sup>-</sup>– $\text{Cu}^{2+}$  was confirmed through  $^1\text{H}$  NMR for dilute NPC solutions, as described in detail in Fig. S5 (ESI<sup>†</sup>).

Transmission electron microscopy (TEM, Fig. 1d–h) and scanning electron microscopy (SEM, Fig. S6f–j, ESI<sup>†</sup>) showed that the nanoparticles of  $\sim 20$  nm in size in PEDOT:PSS increased in size to large agglomerates as the  $\text{Cu}^{2+}$  concentration increased until it reached 40 wt%. At extremely high concentrations (57 wt%) of  $\text{CuCl}_2$ , large needle-like  $\text{CuCl}_2$  crystals were found to form an inhomogeneous composition on the NPC57 film. Similarly, the atomic force microscopy (AFM) image of the NPC films under ambient conditions ( $\sim 24^\circ\text{C}$  and  $\sim 50\%$  RH) (Fig. S6m–q, ESI<sup>†</sup>) showed that the small PEDOT:PSS nanoparticles aggregated to form large agglomerates at a high  $\text{CuCl}_2$  content. At the same time, the roughness of the film increased as the  $\text{CuCl}_2$  content increased. This indicated that  $\text{Cl}^-$  channels could be developed between



the PEDOT-PSSH-Cu complexes. In the high-resolution X-ray diffraction (HRXRD) patterns, NPC films, except for NPC57, exhibited broad peaks with similar  $2\theta$  values at  $21^\circ$  (Fig. S7, ESI†). These results indicate that  $\text{CuCl}_2$  was well dissolved in NPC media up to 40 wt%, which resulted in poor film quality as seen in NPC57, which exhibited the presence of undissociated  $\text{CuCl}_2 \cdot 2\text{H}_2\text{O}$  crystalline peaks. Additionally, the morphologies of the PEDOT:PSS and NPC films were stable for 30 days in optical microscopy images except for NPC57 (Fig. S8, ESI†).

As the Cu atom content increased in the films, the sulfur atom content decreased in the EDS images (Fig. S6f-j, ESI†). Interestingly, there were large Cu-rich regions that were segregated by chloride-rich channels, as shown in the EDS for Cu and Cl atoms, respectively. The boundary channels were  $\sim 20$  nm wide but, were poorly connected in NPC25; however, they became larger, up to  $\sim 60$  nm, and more connected, up to  $\sim 1$   $\mu\text{m}$  long, in NPC40. This indicates the formation of chloride channels upon  $\text{CuCl}_2$  addition.

To prove our concept for anion transport for TE media, the thermovoltage ( $\Delta V$ ) was examined at various temperature gradients ( $\Delta T$ ) to obtain the Seebeck constant for NPC films, as detailed in the ESI†. The PEDOT:PSS film showed a high, positive  $S$  of  $7.5 \text{ mV K}^{-1}$  at 60% RH,<sup>9</sup> but the addition of  $\text{CuCl}_2$  changed it to negative  $S$ , proving that the NPCs are n-type (Fig. 2a and Table 1). As the  $\text{CuCl}_2$  was added to the PEDOT:PSS,  $S$  switched signs, changing from  $7.5 \text{ mV K}^{-1}$  to  $-10.2 \text{ mV K}^{-1}$  at 60% RH. The  $S$  of NPC14 was  $-2.0 \text{ mV K}^{-1}$  at 60% RH and showed a higher negative value as the humidity increased, with a value of  $-5.5 \text{ mV K}^{-1}$  at 80% RH.  $S$  was further decreased as the  $\text{CuCl}_2$  content increased. The highest negative  $S$  was found in NPC40 at 80% RH, with a value of  $-18.2 \text{ mV K}^{-1}$ . Interestingly, NPC40 showed a comparably high negative  $S$  of  $-10.2 \text{ mV K}^{-1}$  under ambient conditions (25  $^\circ\text{C}$  and 60% RH). An increase in the  $\text{CuCl}_2$  content up to 46 wt% (NPC46) resulted in a slightly lower  $S$  of  $-17.7 \text{ mV K}^{-1}$  at 80% RH, and it gradually decreased as the  $\text{CuCl}_2$  content increased. The calculated  $S$  values of the NPC films were obtained using the Grotthuss mechanism<sup>32</sup> at a uniform gradient of temperature as in eqn (1) (detailed in the ESI†).

$$|V_{\text{out}}| = \frac{qE_a d^2}{12\epsilon_0 \epsilon_r k_B T} \frac{\Delta T}{T} \nabla n, \quad (1)$$

where  $q$  is the electron charge,  $E_a$  is the activation energy of ions,  $\epsilon_0$  is the vacuum permittivity,  $\epsilon_r$  is the relative permittivity,  $k_B$  is the Boltzmann constant,  $T$  is the average temperature within the distance  $d$ , and  $\nabla n$  is the concentration gradient of ions. As explained in the ESI†, the calculated  $S$  was  $-5.7$  and  $-18.1 \text{ mV K}^{-1}$  for NPC14 and NPC40, respectively, and these agree well with the experimental values ( $-5.5$  and  $-18.2 \text{ mV K}^{-1}$ ). The optimum content of  $\text{CuCl}_2$  in the film was 40 wt% because excess  $\text{CuCl}_2$  in the film remained as undissociated  $\text{CuCl}_2$  crystals that may block ion transport.

A recent study reported the n-type  $S$  of  $-4 \pm 0.2 \text{ mV K}^{-1}$  for 1-ethyl-3-methylimidazolium ([EMIM]) bis(trifluoro-methylsulfonyl)-imide ([TFSI])/poly(vinylidene fluoride-co-hexafluoropropylene) (PVDF-HFP) polymer gels.<sup>15</sup> The  $S$  of NPC40 in this work is 4.6 times larger than the reported values of  $S$  in the TE films. Such an increase in the  $S$  of the NPC films can be attributed to the high  $\sigma_i$  and the fast  $\text{Cl}^-$  ion mobility in the ion channel being less affected by ionic cross-linked  $\text{Cu}^{2+}$  to  $\text{PSS}^-$  (Fig. S4, ESI†). At the optimized  $\text{CuCl}_2$  content for Cu ion binding with PSS, the free  $\text{Cl}^-$  ions became more mobile through the ion channel, resulting in a higher Soret effect. The  $\text{Cl}^-$  ion-transport number ( $t_i$ ), determined from electrochemical impedance analysis, was over 0.93 at 80% RH for NPC films (Table S1, ESI†).

To identify the contribution from ionic and electronic carriers, electrochemical impedance spectroscopy was performed under an alternating voltage of 0.1 V across the NPC films at various humidity levels (Fig. S9, ESI†). The  $\sigma_i$  was much larger than  $\sigma_e$  (Table 1), therefore, the electronic contribution to TE of NPC seemed quite low. The  $\sigma_i$  increased as the  $\text{CuCl}_2$  content increased. At 60% RH, the  $\sigma_i$  of the NPC14 and NPC40 films were 0.67 and  $1.37 \text{ S m}^{-1}$ , and they increased further as the humidity increased to 3.89 and  $5.26 \text{ S m}^{-1}$  at 80% RH, respectively (Fig. 2b). The NPC57 film initially showed a high  $\sigma_i$ , which may be affected by high instant ion concentration ( $\text{Cl}^-$ ) in aqueous media, as observed in the media having high ion concentration.<sup>27</sup> Increasing the humidity of the environment is known to enhance the ionic transport in PEDOT:PSS. Since  $\text{Cl}^-$  ions readily dissociate from  $\text{Cu}^{2+}$  in PEDOT:PSS, they become highly mobile in humid media and could be influenced by humidity; indeed, the NPC film showed a large dependence of  $\sigma_i$  and  $S_i$  on the humidity as well as the content of  $\text{CuCl}_2$ . Thus, TE from NPCs could be mainly

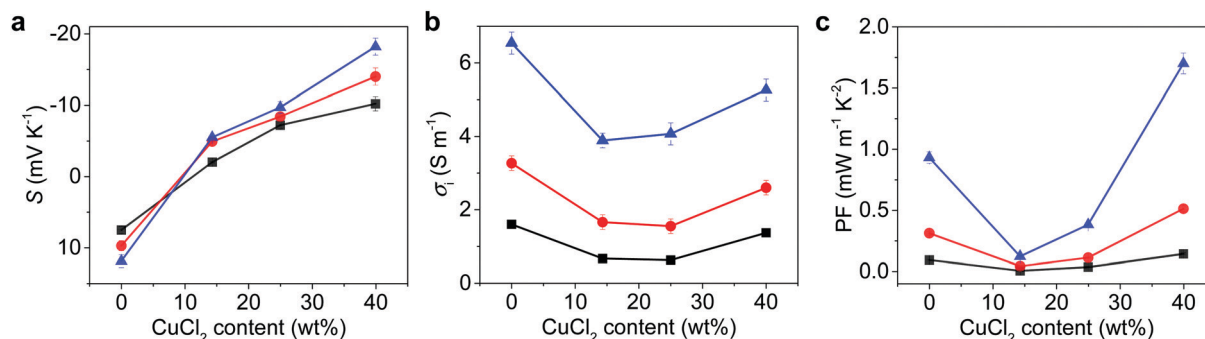


Fig. 2 Thermoelectric parameters of NPC films. (a) Seebeck coefficient, (b) ionic conductivity, and (c) power factor of NPC films at different RH values (%) and  $\text{CuCl}_2$  contents. Black: 60% RH, red: 70% RH, blue: 80% RH. Error bars indicate the s.d. of three experimental replicates.



**Table 1** Summary of the thermoelectric parameters of the NPC films as compared with other TE materials in the literature at room temperature and various humidity levels

Sample	Major <sup>a</sup> carrier, type	RH, %	$\sigma_i^b$ , S m <sup>-1</sup>	$\sigma_e^c$ , S m <sup>-1</sup>	$S^d$ , mV K <sup>-1</sup>	PF <sup>e</sup> , mW m <sup>-1</sup> K <sup>-2</sup>	Stability, day	Ref.
NPC14	I, n	60	0.67	$2.7 \times 10^{-3}$	-2.0	$2.7 \times 10^{-3}$	> 30	This work
		70	1.66	0.018	-4.9	0.04		
		80	3.89	0.012	-5.5	0.12		
NPC25	I, n	60	0.63	0.050	-7.2	0.033	> 30	
		70	1.55	0.12	-8.4	0.11		
		80	4.07	0.13	-9.7	0.38		
NPC36	I, n	80	—	—	-11.2	—	> 30	
NPC40	I, n	60	1.37	0.39	-10.2	0.14	> 30	
		70	2.60	0.63	-14	0.51		
		80	5.26	0.30	-18.2 (-18.1/-18.2)	1.7		
NPC57	I, n	60	26.5	0.66	-8.5	1.9	~ 7	
		70	34.0	1.08	-10.3	3.6		
		80	43.0	0.83	-11.2 (-9.5/-5.4)	5.4 (3.9/1.3)		
PEDOT:PSS:PSSH	I, p	80	12.2	0.03	16.0	3.1	> 30	9
Polymer gel	I, n	—	0.6	—	-4	$9.6 \times 10^{-3}$	—	15
CNT-PEDOT composite	E, n	35–40	—	~ 670	~ -1.25	1.05	~ 17	18
		> 90	~ 5.5	—	~ -7.24	0.29		
		> 90	~ 1	—	-2	$4 \times 10^{-3}$		
AgOH-Nafion	I, n	> 90	—	—	-2	$4 \times 10^{-3}$	—	33
Poly(Ni-ett) film	E, n	—	—	~ 22 700	~ -0.126	~ 0.36	—	19
Hybrid superlattice	E, n	—	—	79 000	-0.078	0.45	—	21
Doped FBDPPV	E, n	—	—	1400	-0.174	$2.8 \times 10^{-3}$	—	34
Ag <sub>2</sub> Se	E, n	—	—	49 700	-0.14	0.987	—	35
C60/TiS <sub>2</sub>	E, n	—	—	~ 39 200	-0.101	~ 0.4	—	36
Superlattice STO	E, n	—	—	140 000	-0.85	101.15	—	37
Superlattice STN/STO	E, n	—	—	62 500	-0.275	4.7	—	38
$\gamma$ -InSe	E, n	—	—	13 700	-0.41	~ 2.3	—	39

<sup>a</sup> Major carrier, I for ionic and E for electronic. <sup>b</sup> Ionic conductivity was determined from the impedance spectroscopy. <sup>c</sup> Electrical conductivity was determined from the impedance spectroscopy. <sup>d</sup> Seebeck coefficients in parentheses indicate the Seebeck coefficients after 1 day/30 days stored at the corresponding humidity. <sup>e</sup> Power factor. Polymer gel: [EMIM][TFSI]/PVDF-HFP polymer gel; CNT-PEDOT composite: sprayed single-walled CNT and PEDOT:FeCl<sub>4</sub> treated by tetrakis(dimethylamino)ethylene for 30 min; hybrid superlattice: TiS<sub>2</sub>/[(hexylammonium)<sub>0.08</sub>(H<sub>2</sub>O)<sub>0.22</sub>(DMSO)<sub>0.03</sub>] film; doped FBDPPV: FBDPPV doped with 5 wt% N-DMBI; Ag<sub>2</sub>Se: Ag<sub>2</sub>Se film on nylon membrane; C60/TiS<sub>2</sub>: 1 wt% C60/TiS<sub>2</sub> nanosheet hybrid film; superlattice STO: superlattice [9 uc SrTiO<sub>3</sub>/1 uc SrTi<sub>0.8</sub>Nb<sub>0.2</sub>O<sub>3</sub>]<sub>20</sub>[9 uc SrTiO<sub>3</sub>]<sub>10</sub>, 2DES, MQW where MQW is the multiple quantum-well; uc is the unit cell, 2DES: 2D electron system; superlattice STN/STO: [1 uc SrTi<sub>0.4</sub>Nb<sub>0.6</sub>O<sub>3</sub>]<sub>11</sub> uc SrTiO<sub>3</sub>]<sub>10</sub> 2DES, ~ 5.3 nm thickness;  $\gamma$ -InSe:  $\gamma$ -phase indium selenide, samples with thickness of 7 nm.

attributed to the ion transport process. Because the concentration of chloride is 7.6 times higher (in NPC40) than that of protons from pristine PEDOT:PSS, the major ion here could be Cl<sup>-</sup>.

The PF of NPC40 was  $1.7 \text{ mW m}^{-1} \text{ K}^{-2}$  at 80% RH, which is 1.9 and 14.8 times higher than that of p-type PEDOT:PSS and n-type NPC14, respectively, under the same conditions (Fig. 2c). NPC57 initially showed a high PF because of high  $\sigma_i$ , but CuCl<sub>2</sub> in the NPC57 was soon crystallized and led to inhomogeneous film as shown in Fig. 1h. Accordingly, the film showed lower PF (Table 1), as the inhomogeneous CuCl<sub>2</sub> crystals may block ion transport. The state-of-the-art PF of polymer-based n-type ionic TE material in the literature was  $9.6 \mu\text{W m}^{-1} \text{ K}^{-2}$ , which was observed from a polymer gel.<sup>15</sup> Compared to this value, the PF of NPC40 was improved by 177 times. Furthermore, the PF of NPC40 was 1.6 times higher than the highest PF ( $1050 \mu\text{W m}^{-1} \text{ K}^{-2}$ ) of the polymer-based n-type electronic material in the literature, which was obtained from a single-walled CNT and PEDOT:FeCl<sub>4</sub> composite treated by tetrakis(dimethylamino)ethylene.<sup>18</sup> These results can be attributed to the large increases in  $S_i$  and  $\sigma_i$ , which may have originated from the free Cl<sup>-</sup> and effective Cl<sup>-</sup> transport through the ion channel in NPC films (Fig. 1a).

For the direct confirmation of Cl<sup>-</sup> transport, an NPC40 film on ITO glass was quickly dried under vacuum (~ 1 mTorr) when the film was producing  $V_{\text{out}}$  of 82 mV at  $\Delta T$  of 4.5 K and 80% RH for 10 min. The film was further dried in an SEM chamber

under high vacuum (~  $10^{-4}$  Torr) (Fig. 3a and Fig. S10, ESI†). Ten points (area of  $4 \times 3 \mu\text{m}^2$ ) were selected for EDS mapping according to the position of the film on hot and cold Peltier devices (Fig. 3b). The atomic% of Cl at different points were plotted and shown in Fig. 3d. Near the boundary of the hot side and gap area, the atomic% of Cl gradually increased, and it sharply decreased toward the cold side near the center of the film. The maximum atomic% (~ 1 mm from the hot edge) was ~ 2 times higher than that of normal points. This result shows clear transport of Cl<sup>-</sup> in the NPC40 film under  $\Delta T$  to explain the high  $S$  and  $V_{\text{out}}$  in one film.

Further Cl<sup>-</sup> transport under  $\Delta T$  was clearly verified through fluorescence imaging, in which *N*-(ethoxycarbonylmethyl)-6-methoxyquinolinium bromide (MQAE) was used as the Cl<sup>-</sup> indicator (Fig. S11, ESI†). Initially, without  $\Delta T$ , the MQAE-stained NPC40 (at 80% RH) showed poor fluorescence contrast as Cl<sup>-</sup> ions were spread over the film (Fig. 3e, g and Fig. S12, ESI†). Interestingly, the NPC40 showed dramatic fluorescence contrast between the hot and cold electrodes. Thus, when electrode 1 (E1) was heated while the electrode 2 (E2) was left cold, the fluorescence intensity was increased at cold E2 while the hot part remained dark (Fig. 3e-ii). This indicates that Cl<sup>-</sup> ions were transferred to the cold side. The temperature of each electrode was reversed to determine whether the fluorescence intensity was higher at the cold electrode (Fig. 3e-g). Furthermore, the



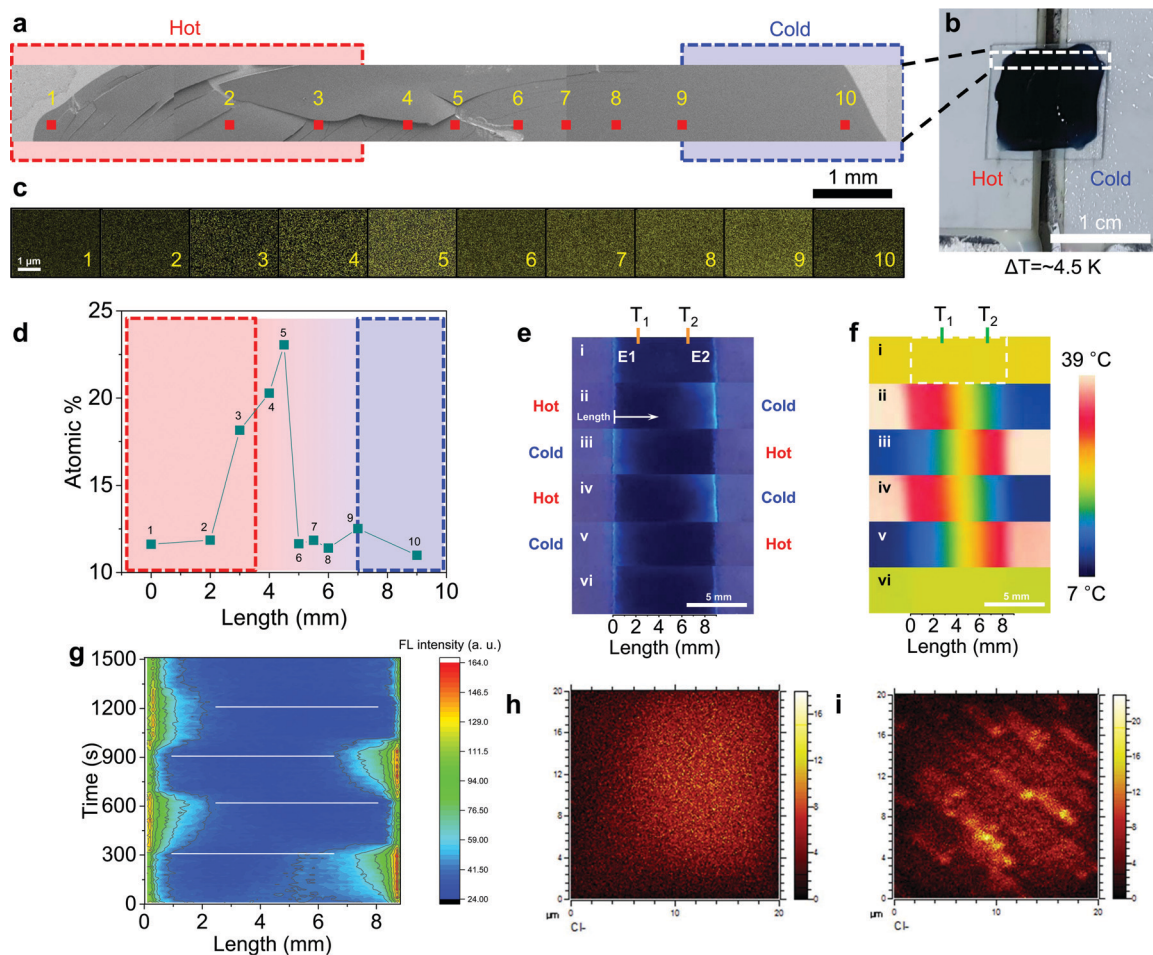


**Fig. 3** A demonstration of ion transport in NPC40 films. (a) SEM image of the NPC40 film dried when the film was producing TE  $V_{\text{out}}$  of 82 mV at  $\Delta T$  of 4.5 K and 80% RH for 10 min. (b) A photograph of the NPC40 film on hot and cold Peltier devices. (c) EDS maps and (d) atomic% of Cl at the ten selected points measured from EDS mapping. (e) Reversible fluorescence switching with repeated heating-cooling cycles of the MQAE-stained NPC40 film under hand-held UV lamp.  $\Delta T$  equals  $T_1 - T_2$ . (i)  $\Delta T = 0$  K (pristine); (ii), (iv)  $\Delta T = 4.5$  K for 5 min; (iii), (v)  $\Delta T = -4.5$  K for 5 min; (vi)  $\Delta T = 0$  K for 5 min. (f) The corresponding thermal images obtained by an IR camera for the samples in (e). (g) The corresponding fluorescence intensity profile over time of (e). ToF-SIMS map of the chlorine distribution on the cross-section surface of the (h) PEDOT:PSS and (i) NPC40 films.

fluorescence switching was reversible by the temperature switching. The confocal image of the NPC40 film showed similar  $\text{Cl}^-$  transport. Thus, the cold part (bottom) of the NPC film was brighter than the hot part (top) as  $\Delta T$  (3 K) was applied. This effect can be explained by the  $\text{Cl}^-$  ion transport from the hot part to the cold part. Additionally, when the temperature difference was reversed, the cold part (top) became brighter than the hot part (bottom) over time. Interestingly, the MQAE-stained NPC40 film showed reversible fluorescence switching with repeated heating-cooling cycles (Fig. S13, ESI<sup>†</sup>). Thermodiffusion of the fluorescent moiety was saturated after  $\sim 1.5$  min. Additionally, this dried film was cross-cut and the ToF-SIMS map of the chlorine distribution on the cross-section surface was measured in a negative ion mode (Fig. 3h, i and Fig. S14, ESI<sup>†</sup>). Bundle-like structures with  $\text{Cl}^-$  clusters were found and the thickness was  $\sim 170$  nm. Furthermore, the  $\text{Cl}^-$  intensity at the cold part was 1.8 times larger than the hot part.

The  $V_{\text{out}}$  of n-type NPC films was linearly dependent on  $\Delta T$  (Fig. 4a) and reproducible under three repeated heating-cooling

cycles, indicating the high stability of the NPC films (Fig. 4b). Additionally, the generated  $V_{\text{out}}$  was well maintained up to 500 s. To determine the output power from NPC40, the film was connected to an external load resistor, and the variations in  $V_{\text{out}}$ , current ( $I_{\text{sc}}$ ), and output power of the NPC40 film were measured at a  $\Delta T$  of 4.5 K and 80% RH. By dividing the cross-sectional area, the output power density of the NPC40 film was maximized to  $0.38 \text{ mW m}^{-2}$  by connecting it with a resistance of  $300 \text{ k}\Omega$  from impedance matching (Fig. S15, ESI<sup>†</sup>). In addition, the specific ( $C_s$ ) and areal capacitance ( $C_a$ ) of the NPC40 film on Au and CNT electrodes were estimated from cyclic voltammograms (Fig. S16a, ESI<sup>†</sup>). The NPC40 film on CNT electrodes showed  $C_s$  and  $C_a$  of  $5.65 \text{ F g}^{-1}$  and  $0.22 \text{ F cm}^{-2}$  at 80% RH, respectively, which are 4.6 times higher than those of the NPC40 film on Au electrodes because of the high surface area of the CNT electrode (Fig. S17, ESI<sup>†</sup>). Additionally, the stability of the NPC40 film on CNT electrodes was investigated as a function of time at 80% RH and  $25^\circ\text{C}$ . The NPC40 film on CNT electrodes was stable for 10 days, maintaining 97.5% of



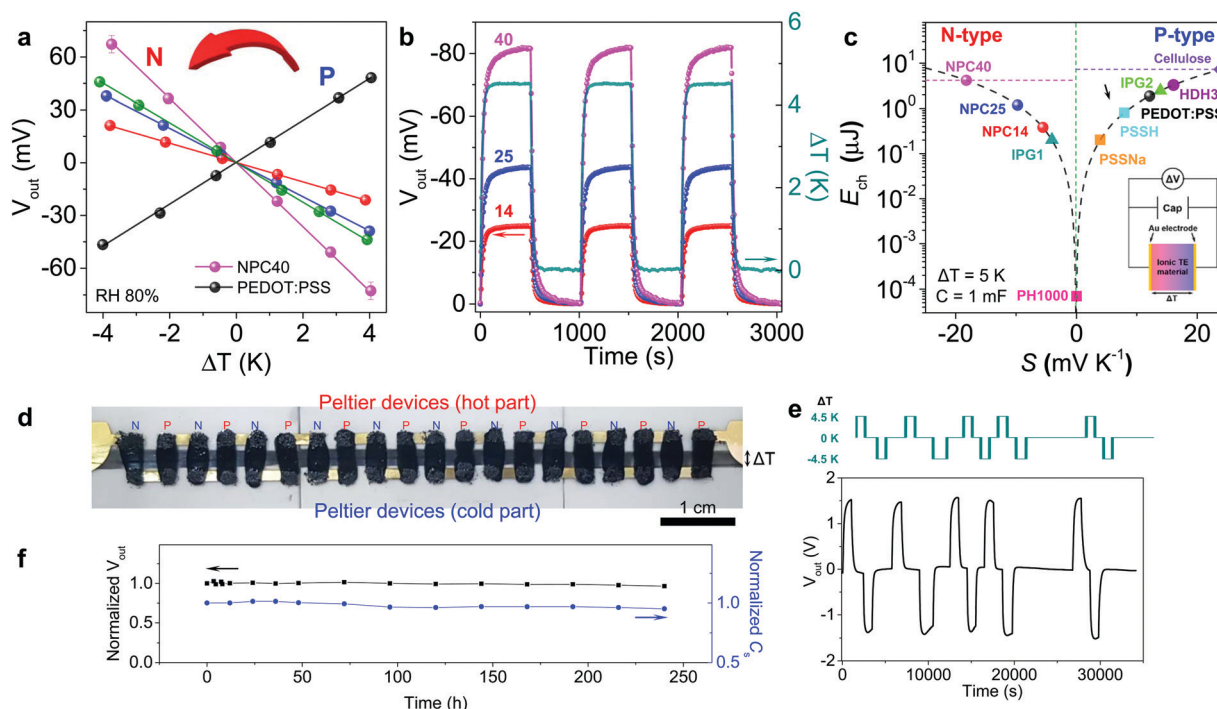


**Fig. 4** Thermoelectric performance of NPC films and a flexible module-type device. (a) Output voltage at different  $\Delta T$  values and 80% RH. The slope of the linear fit of the data for the Seebeck coefficient. PEDOT:PSS (black), NPC14 (red), NPC25 (blue), NPC40 (magenta), and NPC57 (green). (b) Output voltage of NPC films under 10 repeated heating-cooling cycles at  $\Delta T$  of 4.5 K and 80% RH. (c) The charged energy to a capacitor from different thermoelectric materials ( $\Delta T = 5$  K,  $C = 1$  mF).  $E_{ch}$  of cellulose membrane, PSSNa, PSSH, ionic polymer gel (IPG), and HDH30 were calculated from the  $S$  in ref. 8, 9 and 13–15, respectively. Inset: Equivalent circuit for thermal charge-discharge with capacitor. (d) The flexible module-type TE harvester composed of 10 pairs of p–n legs on CNT electrodes. (e) Reproducible output voltage buildup under 10 repeated heating-cooling cycles. (f) Stability testing of the output voltage and specific capacitance for 10 days. The harvester was stored under ambient conditions (25 °C and 50% RH) and measured at a  $\Delta T$  of 4.5 K and 80% RH.

the pristine capacitance from the cyclic voltammograms (Fig. S16b, ESI†).

Fig. 4c shows the current status of electrochemical energy storage ( $E_{ch}$ ) in different n- and p-type TE capacitors, in which the reported  $S$  values were converted into  $E_{ch}$  for a  $\Delta T$  of 5 K and  $C$  of 1 mF for comparison (see details in the ESI†). NPC14, NPC25, and NPC40 had  $E_{ch}$  values of 0.38, 1.2, and 4.1  $\mu\text{J}$  at 80% RH, respectively. The thermal conductivity of the NPC40 was determined as 0.26 and 0.34  $\text{W m}^{-1} \text{K}^{-1}$  at 60 and 80% RH, respectively. Considering the above TE properties,  $ZT$  and theoretical maximum efficiency were calculated as 1.54 and 0.34% at 298 K, a  $\Delta T$  of 4.5 K, and 80% RH. These values are much higher than those of other materials in the literature.<sup>13–15</sup> Compared with p-type HDH30, the  $E_{ch}$  value of NPC40 was 1.3 times higher, which makes it a promising n-type ionic TE material for a module-type flexible TE device.

Taking advantage of the high negative  $S$  and stable voltage generation, NPC40 film was integrated with p-type HDH30 film<sup>9</sup> as a flexible module-type TE harvester. This module-type TE harvester had 10 pairs of p–n legs (each area of  $2 \times 4 \text{ mm}^2$ ) on CNT electrodes (Fig. 4d). The  $V_{out}$  for the module-type TE harvester reached 1.55 V at a  $\Delta T$  of 4.5 K and 80% RH (Fig. 4e). Thus, one pair of p–n legs generated  $\sim 155 \text{ mV}$ , with  $S$  of 34.4  $\text{mV K}^{-1}$ , which is similar to the sum of  $S$  for each n-type (18.2  $\text{mV K}^{-1}$ ) and p-type (16.0  $\text{mV K}^{-1}$ ) film. This is, to our

knowledge, the highest  $S$  (n, p) achieved to date in an organic-based TE module. The  $V_{out}$  showed stable and reproducible build-up under 10 repeated heating-cooling cycles. Additionally, it showed stable  $V_{out}$  and  $C_s$  values with small losses of 3.5% and 5%, respectively, in a stability test for 10 days (Fig. 4f). Such a large and stable  $V_{out}$  build-up without  $V_{out}$  loss was first demonstrated in the module-type TE harvester based on conductive polymers. This module-type TE platform can be used for compact energy harvesting and body-worn or integrated electronics.

## Conclusions

In summary, a high-performance n-type ionic TE film was demonstrated under ambient conditions. The addition of  $\text{CuCl}_2$  in a PEDOT:PSS solution produced free  $\text{Cl}^-$  anions in the ion channel in wet conductive polymer media. The morphology and homogeneity study of the NPC film elucidated PEDOT-rich and PSS-rich parts and ion channels in the NPC media. The NPC40 film showed a surprisingly high negative  $S$  value of  $-18.2 \text{ mV K}^{-1}$  and a PF of 1.7  $\text{mW m}^{-1} \text{K}^{-2}$  at 80% RH, which, to the best of our knowledge, is the highest among conductive polymers. Additionally, a flexible module-type TE harvester with 10 pairs of p–n legs on CNT electrodes showed 1.55 V of  $V_{out}$  at a  $\Delta T$  of 4.5 K and 80% RH. One



pair of p–n legs had  $S$  of  $34.4 \text{ mV K}^{-1}$ , which is similar to the sum of  $S$  for each n-type and p-type legs. From these results, high anion transport in TE materials can be a useful solution for environmentally benign and body-worn electronics.

## Experimental

### Preparation of n-type PEDOT:PSS–CuCl<sub>2</sub> (NPC) films

PEDOT:PSS solutions were prepared by filtering with a PTFE filter (ADVANTEC, pore size of  $0.45 \mu\text{m}$ ) before use. To obtain various n-type PEDOT:PSS–CuCl<sub>2</sub> (NPC) solutions, 14, 25, 40, and 57 wt% CuCl<sub>2</sub> (solid content) were added to the PEDOT:PSS solution and stirred for 5 min under an Ar atmosphere to dissolve all solids. Polyethylene terephthalate (PET) substrates (thickness of  $0.5 \text{ mm}$ ) were topped with gold electrodes patterned by thermal evaporation (thickness of  $100 \text{ nm}$ , width of  $1 \text{ mm}$ , and distance between electrodes of  $3 \text{ mm}$ ). The metal patterned PET substrate was pretreated with ultraviolet/ozone (UVO) for 5 min to generate a hydrophilic surface. Then,  $60 \mu\text{l}$  aliquots of the solutions were drop-cast onto the above pretreated substrate (area of  $0.7 \times 0.7 \text{ cm}^2$ ) and dried under ambient conditions ( $\sim 24^\circ\text{C}$  and  $\sim 50\% \text{ RH}$ ) for 6 h or in an Ar atmosphere chamber ( $\sim 25^\circ\text{C}$ ) with a flow of  $1 \text{ sccm}$  Ar for 1.5 h. For the CNT/Au electrode sample, a CNT dispersion in water ( $0.01 \text{ wt\%}$  of SWCNTs and  $0.1 \text{ wt\%}$  of DWCNTs) was prepared by ultrasonication for 30 min ( $750 \text{ W}$ ,  $40\%$ ,  $2 \text{ s}$  pulse). Next, the CNT solution was dropped on a Au electrode ( $5 \mu\text{l mm}^{-2}$ ) during heating at  $60^\circ\text{C}$  for 1 h to afford a thickness of  $10 \mu\text{m}$ . After water evaporation, the electrodes were rinsed with distilled water before use. For the ionic and electronic measurements, two unsheathed wires were soldered by indium wire to the two metal electrodes using an Ultrasonic Soldering Machine (Mecs Tech Co., Ltd).

### Fabrication of the TE module

PET substrates (thickness of  $0.5 \text{ mm}$ ) were topped with alternating gold electrodes patterned by thermal evaporation (thickness of  $100 \text{ nm}$ , width of  $2 \text{ mm}$ , length of  $6 \text{ mm}$ , and distance between electrodes of  $4 \text{ mm}$ ). Then,  $20 \mu\text{l}$  of the n- and p-type solutions were drop-casted alternatively onto the pretreated substrate above (area of  $2 \times 6 \text{ mm}^2$ ) and dried under ambient conditions ( $\sim 24^\circ\text{C}$  and  $\sim 50\% \text{ RH}$ ) for 6 h. The number of legs was 10 for each type of film. The CNT/Au electrode and wiring were achieved by the same method as above.

## Conflicts of interest

There are no conflicts to declare.

## Acknowledgements

This research was supported by a National Research Foundation (NRF) grant funded by Korean government (Ministry of Science, ICT & Future Planning, MSIP) through the Global Research Lab (GRL: 2016K1A1A2912753) and Creative Materials Discovery Program (2018M3D1A1058536).

## References

- 1 E. Park, E. B. Campbell and R. MacKinnon, *Nature*, 2016, **541**, 500.
- 2 S. Park, S. W. Heo, W. Lee, D. Inoue, Z. Jiang, K. Yu, H. Jinno, D. Hashizume, M. Sekino, T. Yokota, K. Fukuda, K. Tajima and T. Someya, *Nature*, 2018, **561**, 516–521.
- 3 F. Zhang, Y. Zang, D. Huang, C.-A. Di and D. Zhu, *Nat. Commun.*, 2015, **6**, 8356.
- 4 H. Kim, S. Yang, S. R. Rao, S. Narayanan, E. A. Kapustin, H. Furukawa, A. S. Umans, O. M. Yaghi and E. N. Wang, *Science*, 2017, **356**(6336), 430–434.
- 5 B. Russ, A. Glaudell, J. J. Urban, M. L. Chabinye and R. A. Segalman, *Nat. Rev. Mater.*, 2016, **1**, 16050.
- 6 L.-D. Zhao, G. Tan, S. Hao, J. He, Y. Pei, H. Chi, H. Wang, S. Gong, H. Xu, V. P. Dravid, C. Uher, G. J. Snyder, C. Wolverton and M. G. Kanatzidis, *Science*, 2016, **351**, 141–144.
- 7 O. Bubnova, Z. U. Khan, A. Malti, S. Braun, M. Fahlman, M. Berggren and X. Crispin, *Nat. Mater.*, 2011, **10**, 429–433.
- 8 T. Li, X. Zhang, S. D. Lacey, R. Mi, X. Zhao, F. Jiang, J. Song, Z. Liu, G. Chen, J. Dai, Y. Yao, S. Das, R. Yang, R. M. Briber and L. Hu, *Nat. Mater.*, 2019, **18**, 608–613.
- 9 B. Kim, J. Na, H. Lim, Y. Kim, J. Kim and E. Kim, *Adv. Funct. Mater.*, 2019, **29**, 1807549.
- 10 P. Qiu, M. T. Agne, Y. Liu, Y. Zhu, H. Chen, T. Mao, J. Yang, W. Zhang, S. M. Haile, W. G. Zeier, J. Janek, C. Uher, X. Shi, L. Chen and G. J. Snyder, *Nat. Commun.*, 2018, **9**, 2910.
- 11 H. Wang, U. Ail, R. Gabrielsson, M. Berggren and X. Crispin, *Adv. Energy Mater.*, 2015, **5**, 1500044.
- 12 D. Zhao, S. Fabiano, M. Berggren and X. Crispin, *Nat. Commun.*, 2017, **8**, 14214.
- 13 H. Wang, D. Zhao, Z. U. Khan, S. Puzinas, M. P. Jonsson, M. Berggren and X. Crispin, *Adv. Electron. Mater.*, 2017, **3**, 1700013.
- 14 S. L. Kim, H. T. Lin and C. Yu, *Adv. Energy Mater.*, 2016, **6**, 1600546.
- 15 D. Zhao, A. Martinelli, A. Willfahrt, T. Fischer, D. Bernin, Z. U. Khan, M. Shahi, J. Brill, M. P. Jonsson, S. Fabiano and X. Crispin, *Nat. Commun.*, 2019, **10**, 1093.
- 16 Q. Zhang, J. Liao, Y. Tang, M. Gu, C. Ming, P. Qiu, S. Bai, X. Shi, C. Uher and L. Chen, *Energy Environ. Sci.*, 2017, **10**, 956–963.
- 17 Y. Sun, P. Sheng, C. Di, F. Jiao, W. Xu, D. Qiu and D. Zhu, *Adv. Mater.*, 2012, **24**, 932–937.
- 18 H. Wang, J.-H. Hsu, S.-I. Yi, S. L. Kim, K. Choi, G. Yang and C. Yu, *Adv. Mater.*, 2015, **27**, 6855–6861.
- 19 Y. Sun, L. Qiu, L. Tang, H. Geng, H. Wang, F. Zhang, D. Huang, W. Xu, P. Yue, Y.-S. Guan, F. Jiao, Y. Sun, D. Tang, C.-A. Di, Y. Yi and D. Zhu, *Adv. Mater.*, 2016, **28**, 3351–3358.
- 20 C. J. An, Y. H. Kang, H. Song, Y. Jeong and S. Y. Cho, *J. Mater. Chem. A*, 2017, **5**, 15631–15639.
- 21 C. Wan, X. Gu, F. Dang, T. Itoh, Y. Wang, H. Sasaki, M. Kondo, K. Koga, K. Yabuki, G. J. Snyder, R. Yang and K. Koumoto, *Nat. Mater.*, 2015, **14**, 622.



- 22 S. Wang, H. Sun, U. Ail, M. Vagin, P. O. Å. Persson, J. W. Andreasen, W. Thiel, M. Berggren, X. Crispin, D. Fazzi and S. Fabiano, *Adv. Mater.*, 2016, **28**, 10764–10771.
- 23 R. E. Dawson, A. Hennig, D. P. Weimann, D. Emery, V. Ravikumar, J. Montenegro, T. Takeuchi, S. Gabutti, M. Mayor, J. Mareda, C. A. Schalley and S. Matile, *Nat. Chem.*, 2010, **2**, 533.
- 24 S. Guha, F. S. Goodson, L. J. Corson and S. Saha, *J. Am. Chem. Soc.*, 2012, **134**, 13679–13691.
- 25 X. Zhao, D. Madan, Y. Cheng, J. Zhou, H. Li, S. M. Thon, A. E. Bragg, M. E. DeCoster, P. E. Hopkins and H. E. Katz, *Adv. Mater.*, 2017, **29**, 1606928.
- 26 J. Ouyang, *Displays*, 2013, **34**, 423–436.
- 27 P. Vanysek and D. R. Lide, in *CRC Handbook of Chemistry and Physics*, ed. D. R. Lide, CRC Press, Boca Raton, FL, 85th edn, 2005, pp. 5–94.
- 28 J. Ouyang, Q. Xu, C.-W. Chu, Y. Yang, G. Li and J. Shinar, *Polymer*, 2004, **45**, 8443–8450.
- 29 H. Xue and S. Schlick, *Macromolecules*, 1992, **25**, 4437–4441.
- 30 C. S. Fadley, *Surf. Interface Anal.*, 2008, **40**, 1579–1605.
- 31 M. Xue and Y. Tan, *Nanoscale*, 2014, **6**, 12500–12514.
- 32 M. A. Reznikov, *MRS Proc.*, 2011, **1325**, mrss11.
- 33 W. B. Chang, C. M. Evans, B. C. Popere, B. M. Russ, J. Liu, J. Newman and R. A. Segalman, *ACS Macro Lett.*, 2016, **5**, 94–98.
- 34 K. Shi, F. Zhang, C.-A. Di, T.-W. Yan, Y. Zou, X. Zhou, D. Zhu, J.-Y. Wang and J. Pei, *J. Am. Chem. Soc.*, 2015, **137**, 6979–6982.
- 35 Y. Ding, Y. Qiu, K. Cai, Q. Yao, S. Chen, L. Chen and J. He, *Nat. Commun.*, 2019, **10**, 841.
- 36 L. Wang, Z. Zhang, L. Geng, T. Yuan, Y. Liu, J. Guo, L. Fang, J. Qiu and S. Wang, *Energy Environ. Sci.*, 2018, **11**, 1307–1317.
- 37 H. Ohta, S. Kim, Y. Mune, T. Mizoguchi, K. Nomura, S. Ohta, T. Nomura, Y. Nakanishi, Y. Ikuhara, M. Hirano, H. Hosono and K. Koumoto, *Nat. Mater.*, 2007, **6**, 129.
- 38 Y. Zhang, B. Feng, H. Hayashi, C.-P. Chang, Y.-M. Sheu, I. Tanaka, Y. Ikuhara and H. Ohta, *Nat. Commun.*, 2018, **9**, 2224.
- 39 J. Zeng, X. He, S.-J. Liang, E. Liu, Y. Sun, C. Pan, Y. Wang, T. Cao, X. Liu, C. Wang, L. Zhang, S. Yan, G. Su, Z. Wang, K. Watanabe, T. Taniguchi, D. J. Singh, L. Zhang and F. Miao, *Nano Lett.*, 2018, **18**, 7538–7545.

